

A Brief Review on Computational Modeling of Rupture in Soft Biological Tissues

Osman Gültekin and Gerhard A. Holzapfel

Abstract Physiological and pathological aspects of soft biological tissues in terms of, e.g., aortic dissection, aneurysmatic and atherosclerotic rupture, tears in tendons and ligaments are of significant concern in medical science. The past few decades have witnessed noticeable advances in the fundamental understanding of the mechanics of soft biological tissues. Furthermore, computational biomechanics, with an ever-increasing number of publications, has now become a third pillar of investigation, next to theory and experiment. In the present chapter we provide a brief review of some constitutive frameworks and related computational models with the potential to predict the clinically relevant phenomena of rupture of soft biological tissues. Accordingly, Euler-Lagrange equations are presented in regard to a recently developed crack phase-field method (CPFM) for soft tissues. The theoretical framework is supplemented by some recently documented numerical results, with a focus on evolving failure surfaces that are predicted by a range of different failure criteria. A peel test of arterial tissue is analyzed using the crack phase-field approach. Subsequently, discontinuous models of tissue rupture are described, namely the cohesive zone model (CZM) and the extended finite element method (XFEM). Traction-separation laws used to determine the crack growth are described, together with the kinematic and numerical foundations. Simulation of a peel test of arterial tissue is then presented for both the CZM and the XFEM. Finally we provide a critical discussion and overview of some open problems and possible improvements of the computational modeling concepts for soft tissue rupture.

Submitted as a **Book chapter dedicated to Prof. D.R.J. Owen.**

O. Gültekin · G.A. Holzapfel (✉)
Institute of Biomechanics, Graz University of Technology,
Stremayrgasse 16/II, 8010 Graz, Austria
e-mail: holzapfel@tugraz.at

G.A. Holzapfel
Faculty of Engineering Science and Technology, Norwegian University of Science
and Technology (NTNU), 7491 Trondheim, Norway

1 Introduction

Physiological and pathological aspects of soft biological tissues in terms of rupture are of fundamental interest in medical science. In fact, aortic dissection, aneurysms, atherosclerosis, tears in tendons and ligaments and interventional treatments such as balloon angioplasty are common cases where rupture phenomena, mainly driven by changes in the biomechanical environment, are encountered (Lee et al. [40], Holzapfel et al. [32], Sharma and Maffulli [61], Katayama et al. [38], Criado [12], Humphrey and Holzapfel [33] and Kim et al. [39]). This has rendered computational mechanics very important to guide and improve medical monitoring and preoperative planning. Although a relatively large number of fracture models have hitherto been proposed in a diverse range of fields in mechanics, the current review article focuses on those which have been implemented to predict the rupture of soft biological tissues, including the cohesive zone model (CZM), the extended finite element method (XFEM) and the crack phase-field model (CPFM).

Fracture mechanics was pioneered by the works of Griffith [22], Westergaard [70] and Irwin [36]. That happened in the first half of the last century when the concepts of energy release rate and the stress-intensity factor were established as representations of crack growth in solids within the context of linear elastic fracture mechanics (LEFM). In the 1960s, however, researchers turned their attention to crack-tip plasticity wherein significant plastic deformations precede failure. During this time, Dugdale [15] and Barenblatt [4], among others, studied yielding of materials at the crack tip. Later, Rice [59] used a line integral, which became known as the J -integral, to express crack initiation and growth which is basically evaluated along an arbitrary contour near the crack tip. Subsequently, Hutchinson [35] and Rice and Rosengren [60] managed to relate the J -integral to the crack-tip stress fields which indicates that the J -integral can be perceived as a nonlinear stress-intensity parameter as well as an energy release rate. Much of the theoretical foundations of fracture mechanics was formulated by 1980. A more elaborate historical account and details of the concepts can be found in the book by Anderson [1]. With the recent advances in computer technology, computational mechanics has assumed an increasingly significant role in the modeling of material fracture.

CZMs, introduced by Barenblatt [3] and Dugdale [15], consider fracture as a separation of two bulk materials which takes place on a cohesive surface placed in between the bulk element boundaries. The resistance to separation is specified through a cohesive law (traction-separation law). In fact, tractions vanish when the separation (opening displacement) reaches a critical value. This method became particularly appealing for problems where the extent of crack growth or the size of the yielding zone are unknown/not predetermined. Later on, Needleman [55], Xu and Needleman [72] and Camacho and Ortiz [11], among several others, modeled cohesive zones pertaining to the irreversible cohesive laws, adaptive insertion of surface elements, and the dynamic fracture, respectively. The CZM was applied to the fracture of a stenotic artery by Ferrara and Pandolfi [16] using an anisotropic extension of the irreversible cohesive law, as proposed by Ortiz and Pandolfi [56].

Later on, Ferrara and Pandolfi [17] simulated a peel test of a dissected aortic medial strip based on the experimental work of Sommer et al. [66]. The main problems regarding CZMs are the mesh dependency of the results, which can only be resolved through an increase in the finite element size, and the necessity of remeshing in cases when the crack path is not known a priori.

XFEM, developed by Belytschko and co-workers [5, 54], is a technique to deal with fracture without (or with minimal) remeshing. The hallmark of XFEM relies on the local enrichment functions with additional degrees of freedom on the basis of partition of unity finite elements (PUFEM), which resorts to Melenk and Babuška [45]. Moës et al. [54] also incorporated discontinuous displacement fields by using Heaviside functions. Later, Moës and Belytschko [53] combined the CZM and XFEM approaches, whereby the previously employed stress intensity factors and the J -integral methods were replaced by the cohesive laws. The latter modality was then adopted by Gasser and Holzapfel [21] to simulate dissections in a strip of an aorta. The main problem associated with XFEM is that it is rather difficult to predict complex crack patterns, e.g., a crack subject to branching.

In contrast to CZMs and XFEM, CPFEM utterly bypasses the modeling of discontinuities as the 2D crack surface smears out in a volume domain in 3D, as determined by a specific field equation alongside the balance of linear momentum describing the elastic mechanical problem in solids. The well-known limitations, e.g. curvilinear crack paths, crack kinking and branching angles, emanating from the classical theory of fracture mechanics are alleviated through a variational principal of the minimum energy (see Francfort and Marigo [19]), which was followed by a numerical study (Bourdin et al. [8]) using the Γ -convergence, see Braides [10] and Bourdin et al. [9]. In addition, a Ginzburg-Landau type of phase-field evolution was used by Hakim and Karma [26]. The thermodynamically consistent and algorithmically robust formulations of CPFEM were introduced by the seminal works of Miehe and co-workers, [49, 52], and were successfully applied to several coupled multi-field problems ranging from thermo-elastic-plastic fracture to chemo-mechanical fracture (Miehe et al. [47, 48, 51]). The application of CPFEM in biomechanics dates back to Gültekin [23] which was later applied by Gültekin et al. [24, 25] and Raina and Miehe [57] using anisotropic failure criteria. The numerical aspects of aortic dissections in regard to the experimental study of Sommer et al. [66] were also investigated by Raina and Miehe [57] and Gültekin et al. [25].

This book chapter is organized as follows. Section 2 outlines the basics of the variational setup of the coupled mechanical-fracture problem in the sense of CPFEM, featuring the Euler-Lagrange equations, from which emerge the quasi-static force balance of momentum and the evolution of the phase-field. Therein, both rate-independent and rate-dependent formulations are presented. Subsequently, a brief account of anisotropic failure criteria is provided. Next, an overview of numerical examination of the phenomena of aortic dissection using CPFEM is presented. Section 3 is concerned with models that introduce a discontinuous domain due to fracture, namely CZMs and XFEM. A short summary of the traction-separation laws used to determine the crack growth is provided together with the key aspects of the kinematic and numerical foundations. A numerical example of a dissecting aorta

is demonstrated for both the CZM and the XFEM. Finally, Sect. 4 provides a critical discussion and overview of some open problems and possible improvements in modeling concepts for soft tissue rupture.

2 Crack Phase-Field Modeling of Failure in Soft Tissues

This section deals with the CPFM to model fracture of solids at finite strains featuring the primary field variables, namely the crack phase-field d and the deformation map φ in relation to the evolution of the crack and the balance of linear momentum, respectively. An anisotropic arterial tissue comprised of two families of collagen fibers is used as the material. A mixed saddle point principle of the global power balance then yields the Euler-Lagrange equations of the multi-field problem.

2.1 Primary Field Variables of the Multi-Field Problem

Let us consider a continuum body $\mathcal{B} \subset \mathbb{R}^3$ at time $t_0 \in \mathcal{T} \subset \mathbb{R}$ and $\mathcal{S} \subset \mathbb{R}^3$ at time $t \in \mathcal{T} \subset \mathbb{R}$ in the Euclidean space. The finite macroscopic motion of the body is characterized by the bijective deformation map, i.e.

$$\varphi_t(\mathbf{X}) : \begin{cases} \mathcal{B} \times \mathcal{T} & \rightarrow \mathcal{S}, \\ (\mathbf{X}, t) & \mapsto \mathbf{x} = \varphi(\mathbf{X}, t), \end{cases} \quad (1)$$

that transforms a material point $\mathbf{X} \in \mathcal{B}$ onto a spatial point $\mathbf{x} \in \mathcal{S}$ at time $t \in \mathbb{R}^+$, see Fig. 1. As a second primary field variable we introduce the basic geometric mapping for the time-dependent auxiliary crack phase-field d such that

$$d : \begin{cases} \mathcal{B} \times \mathcal{T} & \rightarrow [0, 1], \\ (\mathbf{X}, t) & \mapsto d(\mathbf{X}, t), \end{cases} \quad (2)$$

which interpolates between the intact ($d = 0$) and the ruptured ($d = 1$) state of the material.

2.2 Kinematics

We start with the description of the deformation gradient, i.e.

$$\mathbf{F} = \nabla \varphi, \quad (3)$$

transforming the unit Lagrangian line element $d\mathbf{X}$ onto its Eulerian counterpart $d\mathbf{x} = \mathbf{F}d\mathbf{X}$ (for the relevant nonlinear continuum mechanics used in this chapter see, e.g., the books by Holzapfel [29] and de Souza Neto et al. [14]). Note that $\nabla[\bullet]$ and $\nabla_x[\bullet]$ denote the gradient operators with respect to the reference configuration and the spatial configuration, respectively. The determinant of \mathbf{F} , the Jacobian $J = \det\mathbf{F} > 0$, characterizes the map of an infinitesimal reference volume element to the associated spatial volume element. Furthermore, in this chapter we adopt the formalism in the sense of Marsden and Hughes [44] and equip the two manifolds \mathcal{B} and \mathcal{S} with the covariant reference metric tensor \mathbf{G} and the spatial metric tensor \mathbf{g} transforming the co- and contravariant objects in the Lagrangian and Eulerian manifolds. As a next step, we exploit the multiplicative split of \mathbf{F} into volumetric \mathbf{F}_{vol} and isochoric $\bar{\mathbf{F}}$ parts, as introduced by Flory [18], and write

$$\mathbf{F} = \mathbf{F}_{\text{vol}}\bar{\mathbf{F}} \quad \text{with} \quad \mathbf{F}_{\text{vol}} = J^{1/3}\mathbf{I} \quad \text{and} \quad \bar{\mathbf{F}} = J^{-1/3}\mathbf{F}, \quad (4)$$

where \mathbf{I} is the second-order identity tensor. Subsequently we define the unimodular part of the left Cauchy-Green tensor $\bar{\mathbf{b}}$ as

$$\bar{\mathbf{b}} = \bar{\mathbf{F}}\mathbf{G}^{-1}\bar{\mathbf{F}}^T, \quad (5)$$

which is a strain measure in terms of spatial coordinates. The energy stored in a hyperelastic isotropic material is characterized by the three modified invariants

$$\bar{I}_1 = \text{tr}\bar{\mathbf{b}}, \quad \bar{I}_2 = \frac{1}{2} \left[\bar{I}_1^2 - \text{tr}(\bar{\mathbf{b}}^2) \right], \quad \bar{I}_3 = \det \bar{\mathbf{b}}. \quad (6)$$

The anisotropic structure of biological tissues makes it necessary to consider additional invariants. Therefore, we introduce two reference unit vectors \mathbf{M} and \mathbf{M}' representing the mean fiber orientations, see Fig. 1, and their spatial counterparts as

$$\mathbf{m} = \mathbf{F}\mathbf{M}, \quad \mathbf{m}' = \mathbf{F}\mathbf{M}', \quad (7)$$

which idealizes the micro-structure of the tissue. Subsequently, we can express the related Eulerian form of the structure tensors $\mathbf{A}_{\mathbf{m}}$ and $\mathbf{A}_{\mathbf{m}'}$ as

$$\mathbf{A}_{\mathbf{m}} = \mathbf{m} \otimes \mathbf{m}, \quad \mathbf{A}_{\mathbf{m}'} = \mathbf{m}' \otimes \mathbf{m}'. \quad (8)$$

Finally, we introduce the (physically meaningful) additional invariants

$$I_4 = \mathbf{g} : (\mathbf{m} \otimes \mathbf{m}), \quad I_6 = \mathbf{g} : (\mathbf{m}' \otimes \mathbf{m}'), \quad (9)$$

which measure the squares of stretches along each fiber direction.

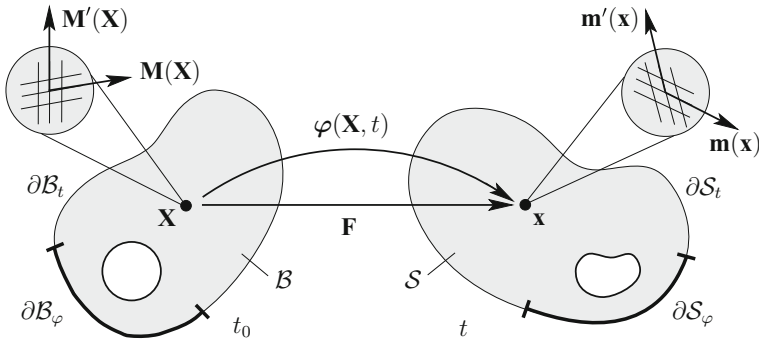


Fig. 1 Nonlinear deformation of an anisotropic solid with the reference configuration $B \in \mathbb{R}^3$ and the spatial configuration $S \in \mathbb{R}^3$. The nonlinear deformation map is $\varphi : B \times \mathbb{R} \mapsto \mathbb{R}^3$, which transforms a material point $X \in B$ onto a spatial point $x = \varphi(X, t) \in S$ at time t . The anisotropic micro-structure of the material point X is rendered by two families of fibers with unit vectors M and M' . Likewise, the anisotropic micro-structure of the spatial point x is described by m and m' , as the spatial counterparts of M and M' (adopted from Gültekin et al. [25])

2.3 Field Equation for Crack Phase-Field in a Three-Dimensional Setting

The multi-dimensional problem of fracture consists of a deformable mechanical domain and a non-deformable domain of the phase-field, as depicted in the Fig. 2a and b, respectively. A sharp crack surface topology at time t can be denoted by $\Gamma(t) \subset \mathbb{R}^2$ in the solid body B , with the definition $\Gamma(d) = \int_{\Gamma} dA$. In contrast, a diffusive crack simply approximates the sharp crack surface by a volume integral in the form of a regularized crack surface functional as

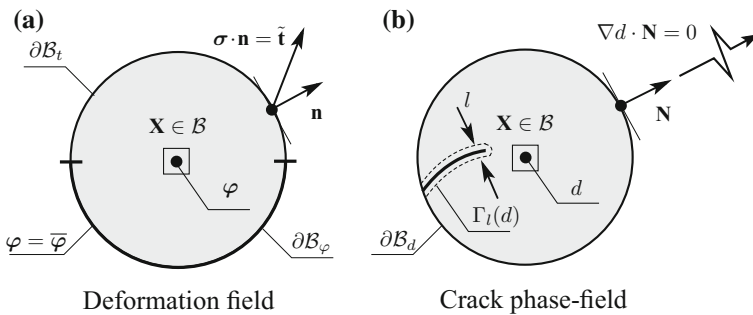


Fig. 2 Multi-field problem: **a** mechanical problem of deformation; **b** evolution of the crack phase-field problem (adopted from Gültekin et al. [25])

$$\Gamma_l(d) = \int_{\mathcal{B}} \gamma(d, \nabla d) dV, \quad \text{where} \quad \gamma(d, \nabla d) = \frac{1}{2l} (d^2 + l^2 |\nabla d|^2), \quad (10)$$

denotes the isotropic volume-specific crack surface while l stands for the length-scale parameter. This can be extended to a class of anisotropic materials via the introduction of an anisotropic volume-specific crack surface γ up to first order, i.e.

$$\gamma(d, \mathbf{Q} \star \nabla d) = \gamma(d, \nabla d), \quad \forall \mathbf{Q} \in \mathcal{G} \subset \mathcal{O}(3), \quad (11)$$

where \mathbf{Q} denotes the rotations in the symmetry group \mathcal{G} , a subset of the orthogonal group $\mathcal{O}(3)$ containing rotations and reflections, and \star denotes an operator. The anisotropic structure is then considered by a second-order structure tensor \mathcal{L} such that

$$\mathcal{L} = l^2 [\mathbf{I} + \omega_{\mathbf{M}} (\mathbf{M} \otimes \mathbf{M}) + \omega_{\mathbf{M}'} (\mathbf{M}' \otimes \mathbf{M}')], \quad (12)$$

which aligns the evolution of the crack according to the orientation of fibers in the continuum using the anisotropy parameters $\omega_{\mathbf{M}}$ and $\omega_{\mathbf{M}'}$, which regulate the transition from weak to strong anisotropy. The anisotropic volume-specific crack surface can now be represented by the alternative form

$$\gamma(d, \nabla d; \mathcal{L}) = \frac{1}{2l} (d^2 + \nabla d \cdot \mathcal{L} \nabla d). \quad (13)$$

We can now state the minimization principle

$$d(\mathbf{X}, t) = \text{Arg} \left\{ \inf_{d \in \mathcal{W}_{\Gamma(t)}} \Gamma_l(d) \right\}, \quad (14)$$

subject to the Dirichlet-type boundary constraint $\mathcal{W}_{\Gamma(t)} = \{d | d(\mathbf{X}, t) = 1 \text{ at } \mathbf{X} \in \Gamma(t)\}$. The Euler-Lagrange equations of the above stated variational principle are then

$$d - \nabla \cdot (\mathcal{L} \nabla d) = 0 \quad \text{in } \mathcal{B} \quad \text{and} \quad \mathcal{L} \nabla d \cdot \mathbf{N} = 0 \quad \text{on } \partial \mathcal{B}, \quad (15)$$

where the non-local effects are considered by the divergence term. In (15)₂ \mathbf{N} is the unit surface normal oriented outward in the reference configuration (for a derivation of the Euler-Lagrange equation see Gültekin [23]).

2.4 Constitutive Modeling of Artery Walls

The effective Helmholtz free-energy function describing the local anisotropic mechanical response of the intact solid assumes a specific form comprising the effective volumetric $U_0(J)$, the isotropic Ψ_0^{iso} and anisotropic Ψ_0^{ani} parts, i.e. (Dal [13])

$$\Psi_0(\mathbf{g}, \mathbf{F}, \mathbf{A}_m, \mathbf{A}_{m'}) = U_0(J) + \Psi_0^{\text{iso}}(\mathbf{g}, \bar{\mathbf{F}}) + \Psi_0^{\text{ani}}(\mathbf{g}, \mathbf{F}, \mathbf{A}_m, \mathbf{A}_{m'}). \quad (16)$$

It needs to be emphasized that in (16) the multiplicative decomposition of the deformation gradient \mathbf{F} is only used for the description of the ground matrix of the artery wall; in other words, we dispense with the multiplicative decomposition for the fiber response. The effective volumetric part in (16) is defined as

$$U_0(J) = \kappa(J - \ln J - 1), \quad (17)$$

while the effective isotropic Ψ_0^{iso} and the effective anisotropic Ψ_0^{ani} parts are functions of the invariant arguments. Thus,

$$\Psi_0^{\text{iso}}(\mathbf{g}, \bar{\mathbf{F}}) = \hat{\Psi}_0^{\text{iso}}(\bar{I}_1), \quad \Psi_0^{\text{ani}}(\mathbf{g}, \mathbf{F}, \mathbf{A}_m, \mathbf{A}_{m'}) = \hat{\Psi}_0^{\text{ani}}(I_4, I_6), \quad (18)$$

which takes on the neo-Hookean and the exponential forms according to Holzapfel et al. [30],

$$\hat{\Psi}_0^{\text{iso}}(\bar{I}_1) = \frac{\mu}{2}(\bar{I}_1 - 3), \quad \hat{\Psi}_0^{\text{ani}}(I_4, I_6) = \frac{k_1}{2k_2} \sum_{i=4,6} \{\exp[k_2(I_i - 1)^2] - 1\}, \quad (19)$$

representing the elastic (and isotropic) response of the ground matrix and the two (distinct) families of collagen fibers, respectively. To give an account of the parameters, κ denotes the penalty parameter enforcing the quasi-incompressible material behavior in (17), while μ indicates the shear modulus in (19)₁. The parameters k_1 and k_2 in (19)₂ denote a stress-like material parameter and a dimensionless parameter, respectively. The anisotropic part contributes to the mechanical response only when a family of fibers is under extension, that is when the invariants $I_4 > 1$ (and $I_6 > 1$). Otherwise the relevant part of the anisotropic function should be excluded from (19)₂. For the derivations of the corresponding constitutive response, i.e. the effective Kirchhoff stress tensor $\boldsymbol{\tau}_0$ and the effective elastic moduli \mathbb{C}_0 see Gültekin et al. [25].

2.5 Variational Formulation Based on Power Balance

We hereby establish the theoretical edifice based on the mixed saddle point principle of the global power balance engendering the coupled Euler-Lagrange equations governing the evolution of the crack phase-field in (i) a rate-dependent and (ii) a rate-independent setting, in addition to the balance of linear momentum and the volumetric constraints. For a degrading continuum the Helmholtz free-energy function becomes

$$\Psi(\mathbf{g}, \mathbf{F}, \mathbf{A}_m, \mathbf{A}_{m'}; d) = g(d)\Psi_0(\mathbf{g}, \mathbf{F}, \mathbf{A}_m, \mathbf{A}_{m'}), \quad (20)$$

where Ψ_0 is the effective Helmholtz free-energy function of the hypothetically intact solid according to (16). The explicit form of the monotonically decreasing quadratic degradation function $g(d)$ is given by

$$g(d) = (1 - d)^2. \quad (21)$$

The function (21) describes the degradation of the tissue as the crack phase-field parameter d evolves, with the following growth conditions:

$$g'(d) \leq 0 \quad \text{with} \quad g(0) = 1, \quad g(1) = 0, \quad g'(1) = 0. \quad (22)$$

Degradation is ensured by the first condition, whereas the second and third conditions set the limits for the intact and the ruptured state of the material. The final condition indicates a saturation as $d \rightarrow 1$. Hence, the volumetric, isotropic and the anisotropic parts of the free-energy function $\Psi = U + \hat{\Psi}^{\text{iso}} + \hat{\Psi}^{\text{ani}}$ for a degenerating material become

$$\begin{aligned} U(J, d) &= g(d)U_0(J), \quad \hat{\Psi}^{\text{iso}}(\bar{I}_1; d) = g(d)\hat{\Psi}_0^{\text{iso}}(\bar{I}_1), \\ \hat{\Psi}^{\text{ani}}(I_4, I_6; d) &= g(d)\hat{\Psi}_0^{\text{ani}}(I_4, I_6), \end{aligned} \quad (23)$$

respectively. In the subsequent treatment, we write the rate of the energy storage functional by considering the time derivative of the isotropic and the anisotropic contributions of (23)_{2,3}, which integrated over the domain gives

$$\mathcal{E}(\dot{\varphi}, \dot{d}; \varphi, d) = \int_{\mathcal{B}} (\boldsymbol{\tau} : \mathbf{g}\nabla_x \dot{\varphi} - f\dot{d}) dV. \quad (24)$$

Therein, we have defined the Kirchhoff stress tensor $\boldsymbol{\tau}$ and the energetic force f such that

$$\boldsymbol{\tau} = g(d)(\boldsymbol{\tau}_0^{\text{iso}} + \boldsymbol{\tau}_0^{\text{ani}}), \quad f = -\partial_d[U(J; d) + \hat{\Psi}^{\text{iso}}(\bar{I}_1; d) + \hat{\Psi}^{\text{ani}}(I_4, I_6; d)]. \quad (25)$$

The Kirchhoff stress tensor $\boldsymbol{\tau}$ is essentially obtained via the effective isotropic and anisotropic Kirchhoff stress tensors $\boldsymbol{\tau}_0^{\text{iso}}$ and $\boldsymbol{\tau}_0^{\text{ani}}$, respectively. Meanwhile, f can be interpreted as the work conjugate of \dot{d} . The external action on the body leads to the external power functional described by

$$\mathcal{P}(\dot{\varphi}) = \int_{\mathcal{B}} \rho_0 \tilde{\gamma} \cdot \dot{\varphi} dV + \int_{\partial \mathcal{B}_i} \tilde{\mathbf{t}} \cdot \dot{\varphi} da, \quad (26)$$

where ρ_0 , $\tilde{\gamma}$ and $\tilde{\mathbf{t}}$ represent the material density, the prescribed body force and the spatial surface traction, respectively. In what follows, the crack dissipation functional \mathcal{D} accounting for the anisotropic dissipated energy in the body is introduced as

$$\mathcal{D}(\dot{d}) = \int_{\mathcal{B}} g_c[\delta_d \gamma(d, \nabla d; \mathcal{L})] \dot{d} dV, \quad (27)$$

where $\delta_d \gamma$ defines the variational derivative of the anisotropic volume-specific crack surface γ according to (Gültekin et al. [24])

$$\delta_d \gamma = \frac{1}{l} [d - \nabla \cdot (\mathcal{L} \nabla d)], \quad (28)$$

and g_c indicates the critical fracture energy (Griffith-type critical energy release rate), see Miehe et al. [49, 52] and Gültekin et al. [24, 25]. Concerning thermodynamics, the dissipation functional has to be non-negative for all admissible deformation processes ($\mathcal{D} \geq 0$), a primary demand of the second law of thermodynamics. This inequality is a priori fulfilled by the local form of the dissipation functional (27) featuring a positive and convex propensity (Miehe et al. [52] and Miehe and Schänzel [50]). The local form of (27) can readily be stated by the principle of maximum dissipation via the following constrained optimization problem

$$g_c[\delta_d \gamma(d, \nabla d; \mathcal{L})] \dot{d} = \sup_{\beta \in \mathbb{E}} \beta \dot{d}, \quad (29)$$

which can be solved by a Lagrange method yielding

$$g_c[\delta_d \gamma(d, \nabla d; \mathcal{L})] \dot{d} = \sup_{\beta, \lambda \geq 0} [\beta \dot{d} - \lambda t_c(\beta; d, \nabla d)], \quad (30)$$

where β is the local driving force, dual to \dot{d} , and λ is the Lagrange multiplier that enforces the constraint. In addition, the threshold function t_c delineating a reversible domain \mathbb{E} is given by

$$\mathbb{E}(\beta) = \{\beta \in \mathbb{R} | t_c(\beta; d, \nabla d) = \beta - g_c[\delta_d \gamma(d, \nabla d; \mathcal{L})] \leq 0\}. \quad (31)$$

Finally, the extended dissipation functional reads

$$\mathcal{D}_\lambda(\dot{d}, \beta, \lambda; d) = \int_{\mathcal{B}} [\beta \dot{d} - \lambda t_c(\beta; d, \nabla d)] dV. \quad (32)$$

2.5.1 Mixed Rate-Independent Variational Formulation Based on Power Balance

The functionals (24), (26), and (32) are brought together for the description of a rate-type potential Π_λ giving rise to the power balance, i.e.

$$\Pi_\lambda = \mathcal{E} + \mathcal{D}_\lambda - \mathcal{P}. \quad (33)$$

On the basis of the rate-type potential (33), the mixed saddle point principle for the quasi-static process states that

$$\{\dot{\varphi}, \dot{d}, \beta, \lambda\} = \text{Arg} \left\{ \inf_{\varphi \in \mathcal{W}_{\dot{\varphi}}} \inf_{\dot{d} \in \mathcal{W}_{\dot{d}}} \sup_{\beta, \lambda \geq 0} \Pi_{\lambda} \right\}, \quad (34)$$

with the admissible domains for the primary variables

$$\mathcal{W}_{\dot{\varphi}} = \{\dot{\varphi} \mid \dot{\varphi} = \mathbf{0} \text{ on } \partial\mathcal{B}_{\varphi}\}, \quad \mathcal{W}_{\dot{d}} = \{\dot{d} \mid \dot{d} = 0 \text{ on } \partial\mathcal{B}_d\}. \quad (35)$$

By considering the variation of Π_{λ} we obtain Euler-Lagrange equations describing the mixed multi-field problem for the rate-independent fracture of an anisotropic hyperelastic solid, i.e.

$$\begin{aligned} 1: & \quad J \operatorname{div}(J^{-1}\boldsymbol{\tau}) + \rho_0 \tilde{\gamma} = \mathbf{0}, \\ 2: & \quad \beta - f = 0, \\ 3: & \quad \dot{d} - \lambda = 0, \end{aligned} \quad (36)$$

along with the Karush-Kuhn-Tucker-type loading-unloading conditions ensuring the principal of maximum dissipation for the case of an evolution of the crack phase-field parameter d , i.e.

$$\lambda \geq 0, \quad t_c \leq 0, \quad \lambda t_c = 0. \quad (37)$$

The elimination of β and λ through (36)_{2,3} and the explicit form of the threshold function t_c results in

$$\dot{d} \geq 0, \quad f - g_c \delta_d \gamma(d, \nabla d; \mathcal{L}) \leq 0, \quad [f - g_c \delta_d \gamma(d, \nabla d; \mathcal{L})] \dot{d} = 0. \quad (38)$$

The first condition ensures the irreversibility of the evolution of the crack phase-field parameter. The second condition is an equality for an evolving crack, which is negative for a stable crack. The third condition is the balance law for the evolution of the crack phase-field subjected to the former conditions.

2.5.2 Mixed Rate-Dependent Variational Formulation Based on Power Balance

In this section we deal with the viscous extension of the variational approach. To this end, we introduce a Perzyna-type viscous extension of the dissipation functional, i.e.

$$\mathcal{D}_{\eta}(\dot{d}, \beta; d) = \int_{\mathcal{B}} [\beta \dot{d} - \frac{1}{2\eta} \langle t_c(\beta; d, \nabla d) \rangle^2] dV, \quad (39)$$

where the viscosity η determines the viscous over-force governing the evolution of \dot{d} . In (39) the positive values for the threshold function t_c are always filtered out owing to the ramp function $\langle x \rangle = (x + |x|)/2$. The corresponding viscous rate-type potential reads

$$\Pi_{\eta} = \mathcal{E} + \mathcal{D}_{\eta} - \mathcal{P}. \quad (40)$$

On the basis of (40), we establish a mixed saddle point principle for the quasi-static process, i.e.

$$\{\dot{\varphi}, \dot{d}, \beta\} = \text{Arg} \left\{ \inf_{\dot{\varphi} \in \mathcal{W}_{\dot{\varphi}}} \inf_{\dot{d} \in \mathcal{W}_{\dot{d}}} \sup_{\beta \geq 0} \Pi_{\eta} \right\}, \quad (41)$$

with the admissible domains for the primary state variables as given in (35). One can retrieve the coupled set of Euler-Lagrange equations for the rate-dependent fracture by simply taking the variation of Π_{η} , which gives

$$\begin{array}{l} 1: J \operatorname{div}(J^{-1} \boldsymbol{\tau}) + \rho_0 \tilde{\gamma} = \mathbf{0}, \\ 2: \beta - f = 0, \\ 3: \dot{d} - \frac{1}{\eta} \langle t_c(\beta; d, \nabla d) \rangle = 0. \end{array} \quad (42)$$

The explicit form of the threshold function t_c recasts the equality (42)₃ in the form

$$f = \eta \dot{d} + g_c \delta_d \gamma(d, \nabla d; \mathcal{L}). \quad (43)$$

The rate-independent setting is recovered for $\eta \rightarrow 0$.

2.6 Crack Driving Function and Failure Ansatz

Focusing on the rate-independent case in (43), for $\eta \rightarrow 0$, we elaborate on the energetic force (25)₂. Accordingly, we substitute the Eqs. (21) and (23) into (25)₂ to arrive at

$$f = 2(1-d)(U_0 + \hat{\Psi}_0^{\text{iso}} + \hat{\Psi}_0^{\text{ani}}) = 2(1-d)\Psi_0. \quad (44)$$

Combining (43) and (44), and considering the rate-independent case together with (28), the following relation holds

$$2(1-d) \frac{\Psi_0}{g_c/l} = d - \nabla \cdot (\mathcal{L} \nabla d). \quad (45)$$

With this notion at hand, one can define the dimensionless crack driving function

$$\bar{\mathcal{H}} = \frac{\Psi_0}{g_c/l}. \quad (46)$$

As discussed by Miehe et al. [51] the dimensionless characteristics of $\bar{\mathcal{H}}$ allows the incorporation of different failure criteria. Subsequently, we postulate that a particular form of the failure Ansatz in accordance with two conditions, i.e. (i) irreversibility of the crack and (ii) positiveness of the crack driving function ensuring that the crack growth solely takes place upon loading. Thus,

$$\mathcal{H}(t) = \max_{s \in [0, t]} [\langle \overline{\mathcal{H}}(s) - 1 \rangle]. \quad (47)$$

The above ramp-type function reckons on the positive values for $\overline{\mathcal{H}}(s) - 1$ and keeps the solid intact below a threshold value, i.e. until the failure surface is reached; therefore, the crack phase-field does not evolve for $\overline{\mathcal{H}}(s) < 1$. We also note that (47) always considers the maximum value of $\overline{\mathcal{H}}(s) - 1$ in the deformation history thereby ensuring the irreversibility of cracking. With these adjustments, (45) now takes on the form

$$2(1 - d)\mathcal{H} = d - \nabla \cdot (\mathcal{L}\nabla d), \quad (48)$$

where the right-hand side of (48) is the geometric resistance to crack whereas the left-hand side is the local source term for the crack growth (Miehe et al. [51]). Bearing this in mind, we recall the rate-dependent case for $\eta \neq 0$, i.e.

$$\boxed{2(1 - d)\mathcal{H} = d - \nabla \cdot (\mathcal{L}\nabla d) + \eta \dot{d}}, \quad (49)$$

which compares to (43) with the replacement of the dimensional energetic force by the dimensionless failure Ansatz, the cornerstone of the crack phase-field model. It needs to be highlighted that the use of a free energy is intrinsic in the phase-field model; therefore the variational formulation does not apply to cases apart from an energy-based criterion. Hence, a stress-based criterion can only be incorporated into (48) or (49) on a rather ad hoc basis.

2.7 Anisotropic Failure Criteria

The dimensionless crack driving function stated in (46) already reflects an energy-based criterion for a general isotropic material. However, it is well known that most soft biological tissues exhibit an anisotropic morphology thereby an anisotropic mechanical response to loading. We herein give a short description of the anisotropic failure criteria which may manifest the rupture phenomena in coherence with clinical observations. For simplicity the ensuing formulations are established according to the assumption that the principal axes of anisotropy lie on the axes of reference. Nonetheless, transformation of stress components can be achieved without much effort. For more details the reader is encouraged to look at Gültekin et al. [25].

2.7.1 Energy-Based Anisotropic Failure Criterion

Two distinct failure processes are assumed to govern the cracking of the ground matrix and the fibers, as suggested by Gültekin et al. [24]. Accordingly, the energetic force in (44) can be additively decomposed into an isotropic part f_{iso} and an

anisotropic part f_{ani} such that

$$f_{\text{iso}} = 2(1-d)(U_0 + \hat{\Psi}_0^{\text{iso}}), \quad f_{\text{ani}} = 2(1-d)\hat{\Psi}_0^{\text{ani}}, \quad (50)$$

which, in their turn, modify (45) into two distinct fracture processes which are superposed to give the following relation

$$(1-d)\bar{\mathcal{H}} = d - \frac{1}{2}\nabla \cdot (\mathcal{L}\nabla d), \quad \text{with} \quad \bar{\mathcal{H}} = \bar{\mathcal{H}}^{\text{iso}} + \bar{\mathcal{H}}^{\text{ani}}, \quad (51)$$

where the dimensionless crack driving functions are defined as

$$\bar{\mathcal{H}}^{\text{iso}} = \frac{U_0 + \hat{\Psi}_0^{\text{iso}}}{g_c^{\text{iso}}/l}, \quad \bar{\mathcal{H}}^{\text{ani}} = \frac{\hat{\Psi}_0^{\text{ani}}}{g_c^{\text{ani}}/l}. \quad (52)$$

Therein, g_c^{iso}/l and g_c^{ani}/l are the critical fracture energies over the length scale for the ground matrix and for the fibers, respectively. Finally, we mention here the modified forms of the rate-dependent and rate-independent cases of the crack evolution, i.e.

$$(1-d)\mathcal{H} = d - \frac{1}{2}\nabla \cdot (\mathcal{L}\nabla d), \quad (1-d)\mathcal{H} = d - \frac{1}{2}\nabla \cdot (\mathcal{L}\nabla d) + \eta\dot{d}. \quad (53)$$

2.7.2 Stress-Based Anisotropic Tsai-Wu Failure Criterion

Composed of a scalar function of two strength tensors, i.e. linear and quadratic forms, the Tsai-Wu criterion (Tsai and Wu [68]) recasts the dimensionless crack driving function $\bar{\mathcal{H}}$ in (46) in regard to the effective Cauchy stress tensor σ_0 in the following form

$$\bar{\mathcal{H}} = \mathbf{T} : \sigma_0 + \sigma_0 : \mathbb{T} : \sigma_0, \quad (54)$$

where \mathbf{T} and \mathbb{T} denote the second- and fourth-order strength tensors, respectively. Through a series of assumptions and simplifications introduced by symmetry relations we end up with the following expression

$$T_{ii} = \frac{1}{(\sigma_i^u)^2} \quad (55)$$

for the diagonal terms of the fourth-order strength tensor related to ultimate normal and shear stresses, where $i \in \{1, \dots, 6\}$. For a comprehensive analysis of the simplifications and assumptions the reader is referred to Tsai and Wu [68] and Tsai and Hahn [67].

2.7.3 Stress-Based Anisotropic Hill Failure Criterion

Considered as an anisotropic extension of the von Mises-Huber criterion, the Hill criterion (Hill [28]) is based on a quadratic form of the dimensionless crack driving function $\overline{\mathcal{H}}$ in (46) such that

$$\overline{\mathcal{H}} = \boldsymbol{\sigma}_0^{\text{vm}} : \mathbb{T} : \boldsymbol{\sigma}_0^{\text{vm}}, \quad (56)$$

where $\boldsymbol{\sigma}_0^{\text{vm}}$ represents the effective von Mises stress tensor. The components of $\boldsymbol{\sigma}_0^{\text{vm}}$ can be defined in terms of

$$\begin{aligned} \sigma_{0_1}^{\text{vm}} &= \sigma_{0_1} - \sigma_{0_2}, & \sigma_{0_2}^{\text{vm}} &= \sigma_{0_2} - \sigma_{0_3}, & \sigma_{0_3}^{\text{vm}} &= \sigma_{0_3} - \sigma_{0_1}, \\ \sigma_{0_4}^{\text{vm}} &= \sigma_{0_4}, & \sigma_{0_5}^{\text{vm}} &= \sigma_{0_5}, & \sigma_{0_6}^{\text{vm}} &= \sigma_{0_6}. \end{aligned} \quad (57)$$

The fourth-order strength tensor \mathbb{T} pertains to the effective normal stresses and shear stresses, as described in Gültekin et al. [25]. The Hill criterion essentially admits a surface of von Mises-Huber-type along the isotropic directions.

2.7.4 Principal Stress Criterion

Developed on the basis of principal stresses the criterion of Raina and Miehe [57] reports on the spectral decomposition of the effective Cauchy stress tensor and takes the positive principal stresses into account, i.e.

$$\boldsymbol{\sigma}_0^+ = \sum_{i=1}^3 \langle \sigma_{0_i} \rangle \mathbf{n}_i \otimes \mathbf{n}_i, \quad (58)$$

where σ_{0_i} denote the effective principal stresses, and \mathbf{n}_i are the corresponding eigenvectors for $i \in \{1, 2, 3\}$. Accordingly, the dimensionless crack driving function $\overline{\mathcal{H}}$ in (46) is rewritten in the following format

$$\overline{\mathcal{H}} = \boldsymbol{\sigma}_0^+ : \mathbb{T} : \boldsymbol{\sigma}_0^+, \quad (59)$$

where the fourth-order strength tensor \mathbb{T} is presented as

$$(\mathbb{T})_{ijkl} = \frac{1}{4\sigma_{\text{crit}}^2} (A_{ik}A_{jl} + A_{il}A_{jk}). \quad (60)$$

Therein, σ_{crit} denotes the reference critical stress associated with uniaxial loading in a certain axis that can be conceptually replaced by an ultimate stress. The second-order anisotropy tensor \mathbf{A} is expressed in index notation for $i, j, k, l \in \{1, 2, 3\}$. Details can be found in Raina and Miehe [57].

2.8 Finite Element Formulation

By considering a discrete time increment $\tau = t_{n+1} - t_n$, where t_{n+1} and t_n stand for the current and previous time steps respectively, we carry out a decoupling of the sub-problems, namely the mechanical and the crack phase-field by appealing to a one-pass operator-splitting algorithm, i.e.

$$\text{ALGO}_{\text{CM}} = \text{ALGO}_{\text{C}} \circ \text{ALGO}_{\text{M}}. \quad (61)$$

Here, such an algorithm yields a decoupling within the time interval and results in partitioned symmetric structures for the two sub-problems. Accordingly, the algorithm for each sub-problem is obtained as

$$(\text{M}) : \begin{cases} J \operatorname{div}(J^{-1}\boldsymbol{\tau}) + \rho_0 \tilde{\boldsymbol{\gamma}} = \mathbf{0}, \\ \dot{d} = 0, \end{cases} \quad (\text{C}) : \begin{cases} \dot{\boldsymbol{\varphi}} = \mathbf{0}, \\ d - \nabla \cdot (\mathcal{L} \nabla d) - 2(1-d)\mathcal{H} + \eta \dot{d} = 0. \end{cases} \quad (62)$$

The algorithm (M) is the mechanical predictor step which is solved for the frozen crack phase-field parameter $d = d_n$, while the algorithm (C) is the crack evolution step for the frozen deformation map $\boldsymbol{\varphi} = \boldsymbol{\varphi}_n$. The remainder of the formulation is summarized in Table 1. A staggered solution procedure is implemented based on a one-pass operator-splitting of the coupled Euler-Lagrange equations on the temporal side whereas a Galerkin-type weak formulation on the spatial side furnishes the finite element formulation along with the rate-dependent setting of the phase-field. Such a solution algorithm successively updates the crack phase-field and the deformation map in a typical time step by means of a Newton-Raphson scheme. For an elaborate treatment of discretization methods and a staggered solution procedure based on a one-pass operator-splitting, the reader is referred to, e.g., Miehe [46], Wriggers [71], Miehe et al. [49] and Gültekin et al. [24, 25].

Table 1 General algorithm for the multi-field problem in $[t_n, t_{n+1}]$

1. Initialization	– At time t_n given: deformation map, phase-field, history field $\boldsymbol{\varphi}_n, d_n, \mathcal{H}_n$
2. Update	– Update the prescribed loads $\tilde{\boldsymbol{\gamma}}, \tilde{\boldsymbol{\varphi}}$ and $\tilde{\mathbf{t}}$ at current time t_{n+1}
3. Compute $\boldsymbol{\varphi}_{n+1}$	– Determine $\boldsymbol{\varphi}_{n+1}$ from the minimization problem of elasticity
ALGO _M	• $G^\varphi = \int_{\mathcal{B}} [\mathbf{g} \nabla_x (\delta \boldsymbol{\varphi}) : \boldsymbol{\tau}] dV - \int_{\mathcal{B}} \delta \boldsymbol{\varphi} \cdot \rho_0 \tilde{\boldsymbol{\gamma}} dV - \int_{\partial \mathcal{B}} \delta \boldsymbol{\varphi} \cdot \tilde{\mathbf{t}} da = 0$
4. Compute history	– Check crack initiation/propagation condition, update history
	• $\mathcal{H}(t_{n+1}) \leftarrow \begin{cases} \mathcal{H}(t_n) & \text{if } \mathcal{H}(t_{n+1}) < \mathcal{H}(t_n) \\ \mathcal{H}(t_{n+1}) & \text{else} \end{cases}$
5. Compute d_{n+1}	– Determine d_{n+1} from the minimization problem of crack topology
ALGO _C	• $G^d = \int_{\mathcal{B}} \delta d [d - 2(1-d)\mathcal{H} + \eta \frac{(d-d_n)}{\tau}] dV + \int_{\mathcal{B}} \nabla(\delta d) \cdot \mathcal{L} \nabla d dV = 0$

2.9 Representative Numerical Examples

We now demonstrate the performance of the proposed model applied to rupture of soft biological tissues. The other aim is to investigate the failure criteria introduced in Sect. 2.7 from a numerical point of view. In particular, the failure surface and the crack propagation associated with distinct failure criteria are compared with each other for rather simple numerical examples.

2.9.1 Numerical Investigation of the Failure Surfaces

We provide an insight to the initiation of the crack with regard to different failure criteria. The example, taken from Gültekin et al. [25], deals with a homogeneous problem with a unit cube discretized by one hexahedral element resolving the analytical solution for the deformation and stress via discarding all non-local effects due to the gradient of the crack phase-field ∇d , see Fig. 3a. As a loading protocol, we first consider uniaxial extension tests along the x -, y - and z -directions with a stretch ratio $\lambda_x = \lambda_y = \lambda_z = 2$ which is followed by a series of planar biaxial deformations in the xy -plane with stretch ratios $\lambda_x : \lambda_y = 2 : 1.1, 2 : 1.25, 2 : 1.5, 2 : 1.75, 2 : 2, 1.75 : 2, 1.5 : 2, 1.25 : 2, 1.1 : 2$. Stretch ratios in the xz - and yz -planes for $\lambda_x : \lambda_z$ and $\lambda_y : \lambda_z$ are applied in an analogous manner as for $\lambda_x : \lambda_y$, see Fig. 3b–d. The tissue is regarded as transversely isotropic consisting of one family of fibers with orientation \mathbf{M} along the x -direction, and it is embedded in the ground matrix. The elastic material parameters and the crack phase-field parameters are listed for each failure criterion in Table 2 (for more details see Gültekin et al. [25]).

Figure 4a–c illustrate the resulting failure surfaces at the instance when $d \neq 0$ for the energy-based criterion, the Tsai-Wu criterion and the principal stress criterion, respectively. The results conspicuously retrieve ellipsoidal failure surfaces. It needs to be emphasized that one can envisage a zone between the macroscopic onset ($d \neq 0$) and the completion ($d = 1$) of the crack in the context of diffusive crack modeling

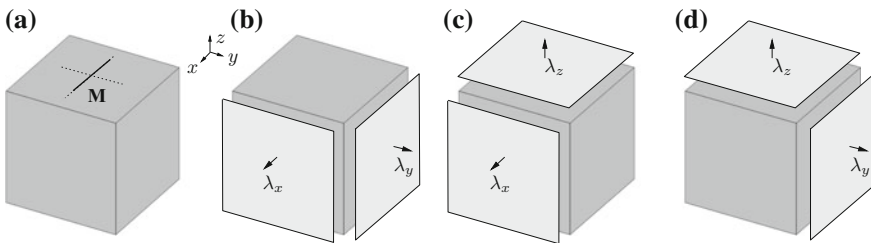


Fig. 3 **a** Unit cube of a transversely isotropic tissue consisting of one family of fibers with orientation \mathbf{M} parallel to the x -direction, initially subjected to uniaxial deformations in the x -, y -, and z -directions followed by a series of planar biaxial deformations **b** in the xy -plane; **c** in the xz -plane; **d** in the yz -plane (adopted from Gültekin et al. [25])

Table 2 Elastic material parameters and crack phase-field parameters for a transversely isotropic material studied in Sect. 2.9.1

Elastic		$\mu = 10 \text{ kPa}$	$g_c^{\text{ani}} = 15 \text{ kPa mm}$	$\alpha_2 = \alpha_3 = 7$
		$k_1 = 20 \text{ kPa}$		
		$k_2 = 1$		
Crack phase-field	Energy-based criterion	$g_c^{\text{iso}} = 5 \text{ kPa mm}$		
	Tsai-Wu criterion	$\sigma_x^u = 140 \text{ kPa}$	$\sigma_y^u = \sigma_z^u = 20 \text{ kPa}$	
	Principal stress criterion	$\sigma_{\text{crit}} = 140 \text{ kPa}$	$\alpha_1 = 1$	
	Hill criterion	$\sigma_x^u = 30 \text{ kPa}$	$\sigma_y^u = \sigma_z^u = 20 \text{ kPa}$	

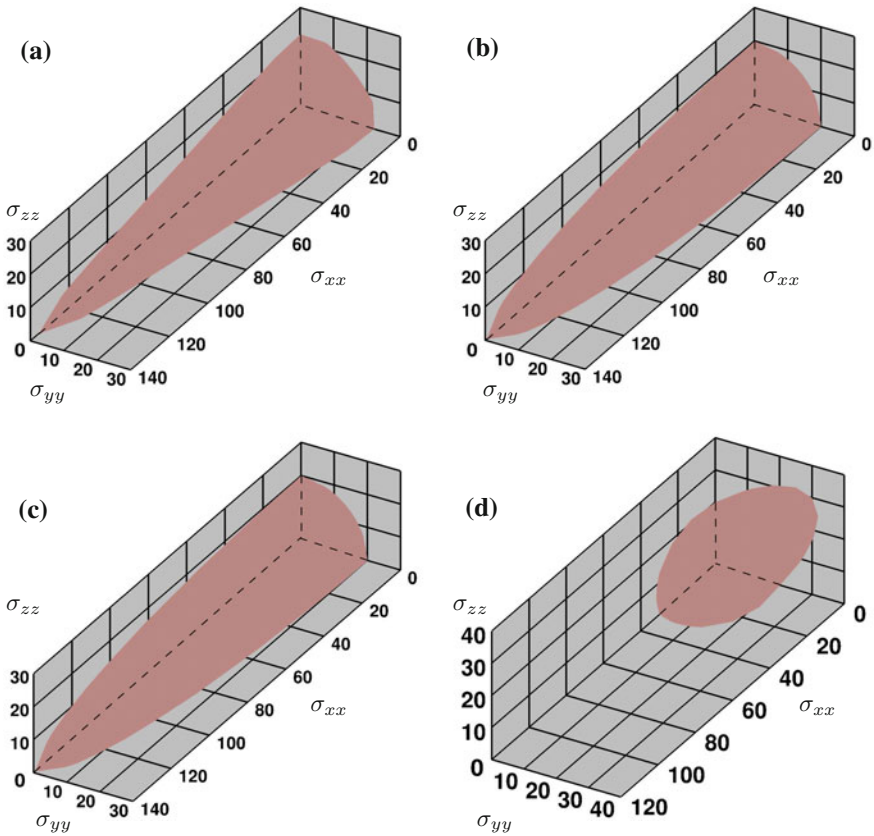


Fig. 4 Failure surfaces in regard to Cauchy stresses σ_{xx} , σ_{yy} and σ_{zz} in kPa at which the failure conditions are satisfied, leading to $d > 0$ for **a** the energy-based; **b** the Tsai-Wu; **c** the maximum principal stress; **d** the Hill failure criterion (adopted from Gültekin et al. [25])

such as the crack phase-field. This example points out the associated macroscopic onset of the crack. Figure 4d shows the failure surfaces obtained at $d \neq 0$ for the Hill criterion (Sect. 2.7.3). In fact, these criteria induce surfaces diverging from being ellipsoidal. In particular, the isotropic failure envelope on the yz -plane eventually becomes discernable, see Fig. 4d, which recovers the von Mises-Huber criterion, as expected.

2.9.2 Peel Test Numerically Analyzed with Different Failure Criteria

Peel tests bear an immense resemblance to the physical phenomena of, e.g., aortic dissections and allow a numerical investigation of the dissection propagation in terms of various failure criteria mentioned in Sect. 2.7. The benchmark with an initial tear models a hypothetical artery comprised of a single family of fibers with orientation \mathbf{M} . The geometric and discrete descriptions of the problem are illustrated in Fig. 5a and b, respectively. The strip was discretized with 2 640 mixed Q1P0 eight-node hexahedral elements. Nodes on the plane at $y = 0$ are fixed in all directions and a horizontal displacement $u_x = 4\text{ mm}$ is incrementally applied at the arms on the top plane in the x -direction. Plain strain conditions are considered in the z -direction. The elastic material parameters are according to Gasser and Holzapfel [21]. The penalty parameter and the length-scale parameter are chosen as $\kappa = 1\,000\text{ kPa}$ and $l = 0.05\text{ mm}$, respectively. The viscosity parameter is adjusted to be $\eta = 1\text{ kPa s}$ for the energy-based criterion and $\eta = 10\text{ kPa s}$ for the stress-based criterion while the anisotropy parameters are selected as $\omega_M = 1.0$ and $\omega_{M'} = 0$ fulfilling weak anisotropy. The other phase-field parameters are taken from Gültekin et al. [25].

The analyses are performed according to the energy-based, the Tsai-Wu, the principal stress and the Hill criterion while the two arms of the strip separated by an initial tear are being pulled in opposite directions, see Fig. 6. It has been observed that the use of stress-based criteria, in general, leads to a crack propagation susceptible to boundary effects not observed in the case of the energy-based criterion.

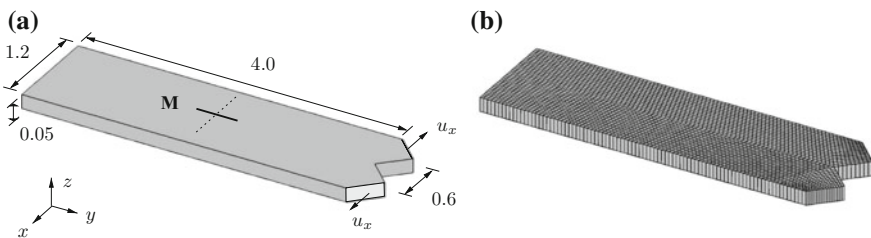


Fig. 5 **a** Geometry of the strip with a single family of fibers with orientation \mathbf{M} in the y -direction, corresponding to the collagenous component of the material. The strip is torn apart by means of a displacement u_x applied at the two arms in the positive and negative x -direction; **b** finite element mesh of the corresponding geometry. Dimensions are provided in millimeters (adopted from Gültekin et al. [25])

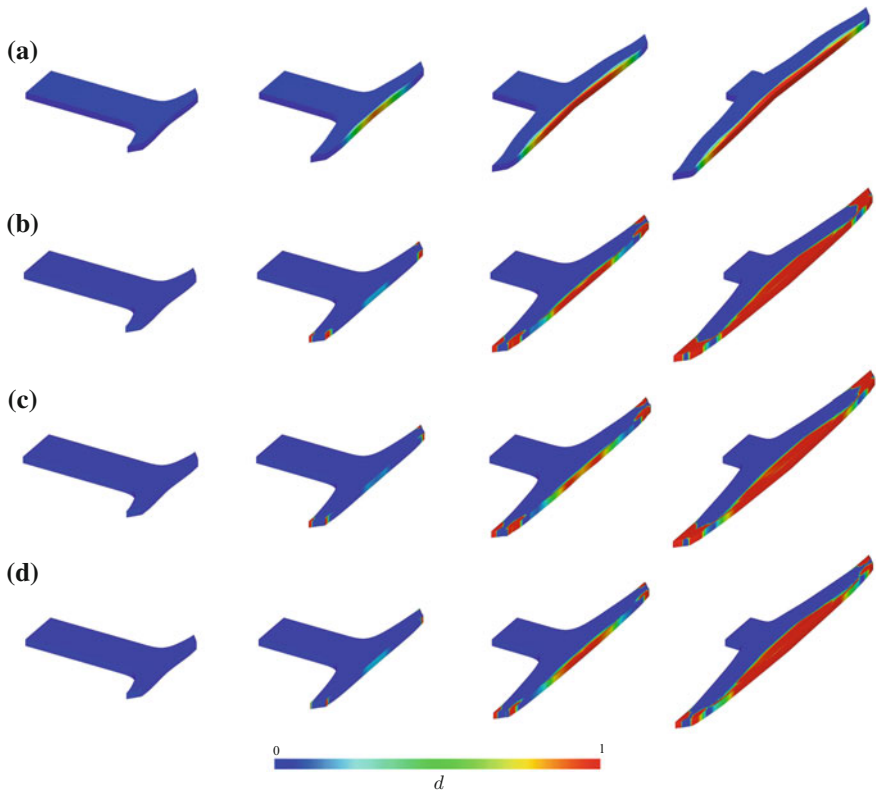


Fig. 6 Evolution of the crack phase-field d for **a** the energy-based; **b** the Tsai-Wu; **c** the principal stress criterion; **d** the Hill criterion, as the arterial tissue with an initial tear is being pulled in two opposite directions (adopted from Gültekin et al. [25])

We close this section by providing a short discussion on the study by Raina and Miehe [57] in which the phase-field of fracture is used to simulate the delamination of the aortic media with the principal stress criterion imparted in Sect. 2.7.4. Although the overall problem setup is akin to the one explained in this section, the finite element mesh comprises of 7 000 displacement-based four-noded quadrilateral elements in 2D. The selected material parameters agree favorably with the parameters identified by Gasser and Holzapfel [21]. Figure 7 shows the contours of the phase-field parameter d at different stages of the deformation, while Fig. 8 provides the load per unit width on one side of the pre-crack at the top line versus the displacement. A good agreement of the plot with the average experimental curve identified by Sommer et al. [66] is discernable.

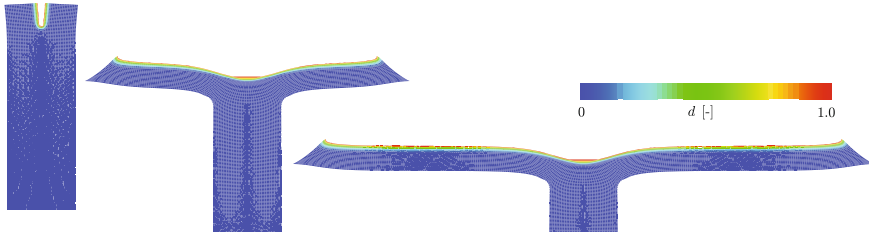
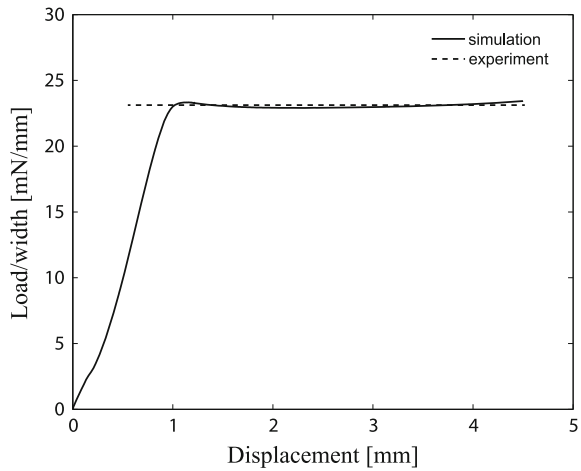


Fig. 7 Contours of the crack phase-field d illustrate the crack propagation in the deformed configuration (adopted from Raina and Miehe [57])

Fig. 8 Plot of load per unit width on one side of the pre-crack at the *top line* against the applied displacement, which is compared with the average experimental data from Sommer et al. [66] (adopted from Raina and Miehe [57])



3 Discontinuous Models of Rupture in Soft Biological Tissues

Endeavors were made to obtain a variational framework for the XFEM and the CZM. In the XFEM, cracks are represented by the enriched nodes enabling asymptotic and discontinuous fields through additional degrees of freedom. CZMs are, however, described by (surface-like) interface elements compatible with general finite element discretization. The concept of cohesive law and XFEM are combined in Moës and Belytschko [53] so that tractions on the crack surface are governed by a traction-separation law. This mixed concept was implemented to model the dissection of an aorta in Gasser and Holzapfel [21] along with the PUFEM. In the forthcoming sections we describe this approach and exploit the mixed saddle point principle. Model implementations are verified by finite element analyses of an abdominal aortic media subject to delamination (mode-I), in accordance to Gasser and Holzapfel [21] and Ferrara and Pandolfi [17].

3.1 Discontinuous Kinematics

Let us assume a continuum body $\mathcal{B} \subset \mathbb{R}^3$ at time $t_0 \in \mathcal{T} \subset \mathbb{R}$ and $\mathcal{S} \subset \mathbb{R}^3$ at time $t \in \mathcal{T} \subset \mathbb{R}$ in the Euclidean space. In view of the entire domain, we assume a strong discontinuity surface $\partial\mathcal{B}_d$ and $\partial\mathcal{S}_d$ in the reference and the spatial configuration, see Fig. 9. The discontinuity separates \mathcal{B} into two subdomains \mathcal{B}_+ and \mathcal{B}_- located in the reference configuration rendering the features $\partial\mathcal{B}_d \cap \mathcal{B}_+ = \emptyset$, $\partial\mathcal{B}_d \cap \mathcal{B}_- = \emptyset$ and $\partial\mathcal{B}_d \cup \mathcal{B}_+ \cup \mathcal{B}_- = \mathcal{B}$. Their spatial counterparts are delineated by $\partial\mathcal{S}_d$, \mathcal{S}_- and \mathcal{S}_+ . The orientations of a material point \mathbf{X}_d and the related spatial point \mathbf{x}_d located on the discontinuous surfaces are characterized by their normal vector \mathbf{N}_d and \mathbf{n}_d , respectively. The essential and the neutral boundary conditions with respect to the reference and spatial configurations are shown in Fig. 9.

Next, we rephrase the deformation map and introduce an additive split of φ into a compatible part φ_c and an enhanced part φ_e , see Simo et al. [65] and Armero and Garikipati [2]. Thus,

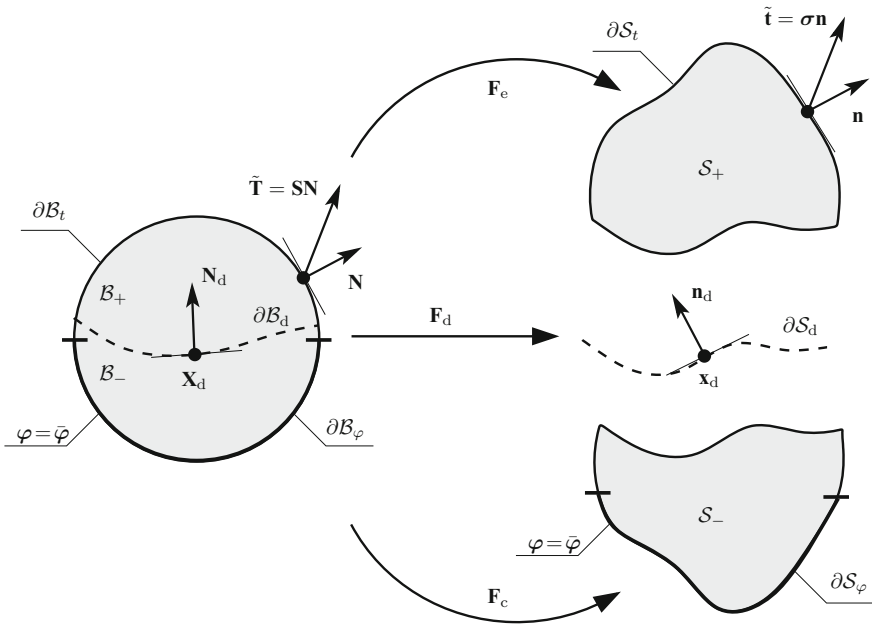


Fig. 9 Discontinuous kinematics representing the reference configuration $\partial\mathcal{B}_d \cup \mathcal{B}_+ \cup \mathcal{B}_- = \mathcal{B}$ and the spatial configuration $\partial\mathcal{S}_d \cup \mathcal{S}_+ \cup \mathcal{S}_- = \mathcal{S}$ of a body subject to the essential and the neutral boundary constraints with the associated deformation gradients \mathbf{F}_d , \mathbf{F}_e and \mathbf{F}_c . Surface tractions on the body surface are denoted by $\tilde{\mathbf{t}}$ (spatial) and $\tilde{\mathbf{T}}$ (referential) with respect to the Cauchy stress tensor $\boldsymbol{\sigma}$ and the second Piola–Kirchhoff stress tensor \mathbf{S} along with the unit normal vectors \mathbf{n} (spatial) and \mathbf{N} (referential). The cohesive tractions on the cohesive surfaces are related to \mathbf{n}_d , the unit spatial normal on $\partial\mathcal{S}_d$

$$\varphi = \varphi_c + \mathcal{H}\varphi_e, \quad (63)$$

where \mathcal{H} denotes the Heaviside function, with values 0 and 1 associated with $\mathbf{X} \in \mathcal{B}_-$ and $\mathbf{X} \in \mathcal{B}_+$, respectively. The assumption that $\partial\mathcal{S}_d$ is the map of $\partial\mathcal{B}_d$ enables the introduction of an average deformation gradient \mathbf{F}_d which resorts to Wells [69], i.e.

$$\mathbf{F}_d = \nabla\varphi_c + \frac{1}{2}\varphi_e \otimes \mathbf{N}_d, \quad (64)$$

where the spatial discontinuity normal \mathbf{n}_d is defined by a contravariant push-forward of the normal vector \mathbf{N}_d such that

$$\mathbf{n}_d = \frac{\mathbf{F}_d^{\text{T}-1}\mathbf{N}_d}{|\mathbf{F}_d^{\text{T}-1}\mathbf{N}_d|}, \quad (65)$$

which gives the preferred direction for anisotropic traction-separation laws. Additionally, we define the compatible deformation gradient \mathbf{F}_c as

$$\mathbf{F}_c = \nabla\varphi_c \text{ from } \mathcal{B}_- \text{ to } \mathcal{S}_-, \quad (66)$$

and the enhanced deformation gradient \mathbf{F}_e as

$$\mathbf{F}_e = \nabla\varphi_c + \nabla\varphi_e \text{ from } \mathcal{B}_+ \text{ to } \mathcal{S}_+. \quad (67)$$

3.2 Traction-Separation Law

The theory of standard dissipative solids treated via potential-based models are well-established by Biot [7] and Halphen and Nguyen [27], among others. Accordingly, Ortiz and Pandolfi [56] postulated the general form of an objective free-energy density per unit undeformed area $\partial\mathcal{B}_d$ which can be interpreted as a cohesive potential or elastic energy stored in the cohesive surfaces, see, e.g., Xu and Needleman [72]. The constitutive law for the cohesive surface is conjectured to be a phenomenological relation between the traction and the displacement jump across the surface. The general form reads

$$\phi = \hat{\phi}(\mathbf{u}_d, d), \quad (68)$$

where \mathbf{u}_d is referred to as the discontinuous displacement representing the displacement jumps, while d is an internal scalar variable accounting for damage. Now, we give an account for two particular forms of this cohesive potential.

3.2.1 Isotropic Cohesive Law

Gasser and Holzapfel [21] uses an isotropic particularization of the cohesive potential according to

$$\phi = \hat{\phi}(i_1, d) = \frac{t_0}{2d} \exp(-ad^b) i_1, \quad (69)$$

where $i_1 = \mathbf{u}_d \cdot \mathbf{u}_d$ defines the first invariant, t_0 denotes the cohesive tensile strength whereas a and b are non-negative parameters which retrieve the softening response of the material based on mode I fracture. Then the cohesive traction \mathbf{t}_d is defined by

$$\mathbf{t}_d = \partial_{\mathbf{u}_d} \phi = \frac{t_0}{2d} \exp(-ad^b) \mathbf{u}_d. \quad (70)$$

Details about the calculation of the cohesive traction and how to extend it to the anisotropic case can be found in Gasser and Holzapfel [20, 21].

3.2.2 Anisotropic Cohesive Law

Ferrara and Pandolfi [16] implement cohesive laws by postulating specific forms of the cohesive potential as, e.g.,

$$\phi = \hat{\phi}(u_{d,1}, u_{d,2}, u_{d,n}, d), \quad (71)$$

where the opening displacements are introduced as

$$u_{d,1} = \mathbf{u}_d \cdot \mathbf{m}, \quad u_{d,2} = \mathbf{u}_d \cdot \mathbf{m}', \quad u_{d,n} = \mathbf{u}_d \cdot \mathbf{m}_n. \quad (72)$$

Therein, \mathbf{m} and \mathbf{m}' designate the unit vectors representing the mean fiber orientations on $\partial\mathcal{S}_d$ (compare with (7)), with their normal component $\mathbf{m}_n = \mathbf{m} \times \mathbf{m}'$. Then, the cohesive traction \mathbf{t}_d is given by

$$\mathbf{t}_d = \partial_{\mathbf{u}_d} \phi = \partial_{u_{d,1}} \hat{\phi} \mathbf{m} + \partial_{u_{d,2}} \hat{\phi} \mathbf{m}' + \partial_{u_{d,n}} \hat{\phi} \mathbf{m}_n. \quad (73)$$

For further simplifications on the cohesive tractions the interested reader is encouraged to see the papers by Ortiz and Pandolfi [56] and Ferrara and Pandolfi [16].

3.3 Finite Element Formulation

The above elucidated mixed modeling (XFEM/PUFEM and CZM for cohesive crack growth) requires that the discontinuities at the crack tip are adequately described by enriching functions such as \mathcal{H} . The displacement field \mathbf{u} is, e.g., interpolated as

$$\mathbf{u} = \sum_{I=1}^{n_{\text{elem}}} N^I \mathbf{u}_c^I + \mathcal{H} \sum_{I=1}^{n_{\text{elem}}} N^I \mathbf{u}_e^I, \quad (74)$$

where N^I denotes the standard (polynomial) interpolation functions with the index I running from 1 to n_{elem} , the number of nodes per element. Therein, \mathbf{u}_c and \mathbf{u}_e indicate the matrix notation of the associated *compatible* and *enhanced* nodal displacement vectors. An important aspect is that the sum of the shape functions must be unity, see Melenk and Babuška [45]. What follows is a standard Galerkin procedure of the problem at hand and the corresponding linearization. It should be noted that as the element stiffness matrix generally becomes non-symmetric, the application of appropriate solvers are indispensable if a quadratic rate of convergence is sought. Details in regard to finite element formulations and their implementations can be found in Gasser and Holzapfel [20, 21].

3.4 Representative Numerical Examples

For the sake of comparison, numerical examples handling the peel test, based on the experimental data of Sommer et al. [66], are presented.

3.4.1 Analysis of a Peel Test According to Gasser and Holzapfel [21]

The contribution [21] uses both XFEM and CZM in order to model a 3D medial aortic strip with geometry and boundary conditions by analogy with Fig. 5. Two families of collagen fibers oriented by an angle of $\pm 5^\circ$ with respect to the circumferential direction manifests the morphology of the tissue. The finite element mesh consists of 9 993 standard tetrahedral elements and involves a refinement around the regions where the crack growth is expected.

The required elastic parameters are accommodated from Holzapfel et al. [31], whereas the cohesive materials are identified according to the experimental data by Sommer et al. [66]. Therein, the dissection failure response of the media, albeit subject to a rather large standard deviation, is found to be anisotropic as the load required to dissect a strip in the longitudinal direction is higher than that in the circumferential direction (35.0 ± 16.0 vs. 23.0 ± 3.0 mN/mm). The cohesive law used here, see Sect. 3.2.1, delineates an isotropic failure where only the tensile strength normal to the cohesive surface is taken into account.

Computations are performed by using approximately 200 displacement increments and the non-symmetric system of algebraic equations are monolithically handled by a direct solver. The distribution of the radial component $\sigma_r = \mathbf{r} \cdot \boldsymbol{\sigma} \cdot \mathbf{r}$ of the Cauchy stress, with r being the spatial radial direction vector, is demonstrated in Fig. 10. Thereby five different stress states are illustrated which are labeled as (a)–(e). The corresponding load-displacement response is provided via Fig. 11. Upon

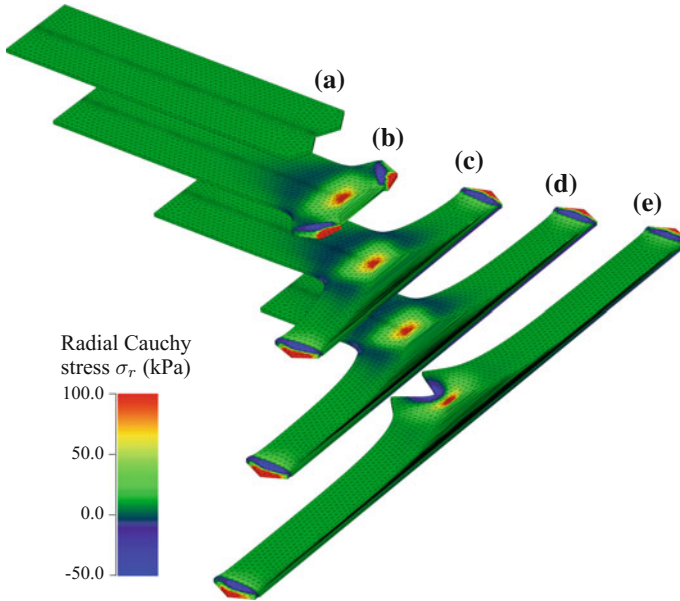
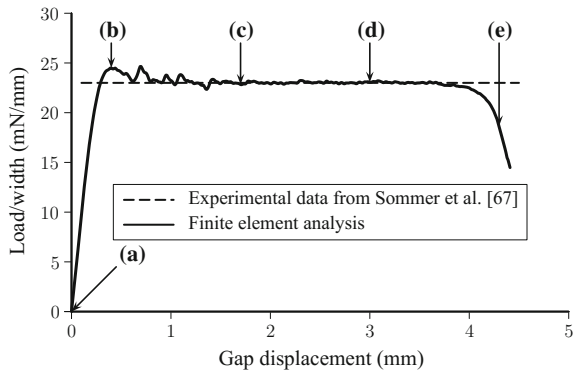


Fig. 10 Spatial distribution and evolution of the radial Cauchy stress σ_r during the propagation of a dissection within a strip of an aortic media (adopted from Gasser and Holzapfel [21])

Fig. 11 Comparison of the (average) experimental load/width with the computed load/width required to propagate a dissection in an aortic human media (adopted from Gasser and Holzapfel [21])



exceeding a threshold value of the load, the response starts to exhibit an oscillatory behavior followed by a gradual degradation after a gap displacement of 4 mm. The plateau region obtained through numerical analysis is in accordance with the experimental data.

3.4.2 Analysis of a Peel Test According to Ferrara and Pandolfi [17]

The study [17] applies the cohesive zone approach to handle a 3D medial aortic strip with geometry and boundary conditions by analogy with Fig. 5. The strip represents a specimen cut out in the circumferential direction with two families of fibers defined by an angle $\pm 5^\circ$ with respect to the circumferential axis. In order to study the effect of the mesh size, the geometry is discretized by a coarse, a medium, and a fine mesh with 10-node standard tetrahedral elements, respectively. The material parameters for the hyperelastic model and the anisotropic cohesive law can be found in Ferrara and Pandolfi [17]. Although the anisotropic cohesive law is employed according to Sect. 3.2.2, problems related to a higher degree of anisotropy occurred which resulted to a breakage of the arms due to bending. This undesired behavior can only be evaded by restricting the crack path along the middle surface of the 3D model.

Figure 12 shows the deformed configurations of three snapshots as the two arms are stretched apart, and the contour levels indicate (a) the first and (b) the second principal Cauchy stress, respectively. As a matter of fact, the second principal Cauchy stress represents the normal component of the stress to the dissecting plane. Figure 13 shows the relationship between the force/width and the total separation of the two arms. The asymptotic behavior of the numerical results is verified through the implementation of three simulations with three different mesh sizes. It is found that the remarkable decrease in the amplitude of the oscillations upon reaching the plateau region is achieved with the finer mesh which resolves the characteristic length scale. Besides, the average pulling force per unit width of 28 mN/mm falls in the range described by experimental data.

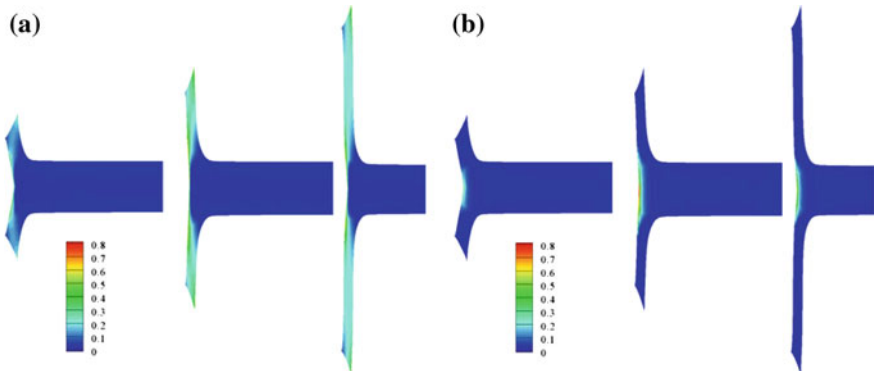
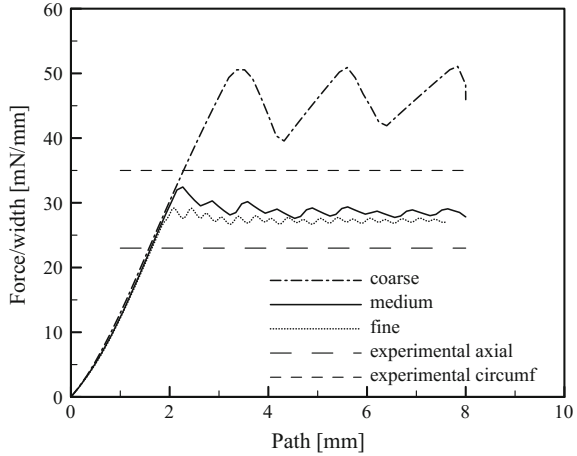


Fig. 12 Evolution of the dissection at three different stages: onset of the dissection, 2 and 4 mm of imposed displacement. Contour levels in MPa refer to **a** the first and **b** the second principal Cauchy stress. With reference to the arterial geometry, the second principal stress corresponds to the radial component (adopted from Ferrara and Pandolfi [17])

Fig. 13 Effects of the mesh size on the numerical simulation of the artery dissection, and comparison with the experimental data from Sommer et al. [66] (adopted from Ferrara and Pandolfi [17])



4 Discussion

Apart from the traditional finite element method relying on mesh-based discretization of the spatial domain, other methods that do not rely on finite element discretization such as meshfree methods based on peridynamic models (Silling [63] and Silling and Askarib [64]), the element-free Galerkin method (Belytschko et al. [6]), and smoothed particle hydrodynamics (Libersky and Petschek [42]), have recently been applied to soft tissue mechanics, see, e.g., Jin et al. [37] and Rausch et al. [58]. The study of Rausch et al. [58] simulated the delamination of an aortic strip according to the experiments performed by Sommer et al. [66], and demonstrated a qualitative agreement of the numerical results with experimental data. Nonetheless, it is also worth mentioning that meshless methods, when utilized in the finite strain context, may require several expedients to suppress non-physical results, e.g., local viscosity augmented to hyperelasticity models to help stabilize the solution, or tracking of free surface particles in order to impose traction-free responses.

Ferrara and Pandolfi [17] adjusted the cohesive law in order to prevent the breakage of the arms and to capture a physically relevant peeling which occurs at the middle of the pre-cracked region. It is worth mentioning that such interventions are not required for the CPFEM when an energy-based failure criterion is used. Apart from that, in both CZM and XFEM, due to their discontinuous setting, the allowed crack paths are prescribed to be along the middle surface of the geometry which render these approaches impractical for complex geometrical and morphological situations as, e.g., a 3D model of dissection propagating through an ascending aorta. It also needs to be emphasized that the presented approaches focus only on the mechanical fracture of solids/tissues, and they completely ignore the intricate feed-back mechanism between the mechanical and the biochemical environment of tissues which may evoke bio-chemo-mechanical fracture.

The mechanical behavior of arterial walls before and after crack initiation is very much dependent on the local variability of collagen, and on the presence of micro-defects and micro-calcifications, see, e.g., Marino and Vairo [43] and Hutchesson et al. [34]. On the top of that, the hierarchical structure of collagen fibers, the main contributor of the mechanical response of soft tissues, is evident from morphological investigations (Sherman et al. [62]). Hence, multi-scale approaches to rupture of soft tissues may provide more physically relevant and holistic approximations than the above-stated macro models.

There is a pressing need for more advanced computational models that can predict the propagation of cracks and the ultimate rupture of soft biological tissues resulting from atherosclerotic plaques, aneurysms, aortic dissection etc. based on clinically available patient-specific data. Such models should also be informed by the underlying mechanobiology of, e.g., the lipid absorbing leukocytes (Libby et al. [41]), matrix-metalloproteinases, Marfan's syndrome, to name but a few (Humphrey and Holzapfel [33]). Growth and remodeling of lesions triggered by mechanobiology should also be taken into account. The focus of modeling and simulation should be more on the tissue structure rather than on a phenomenological description, and should move towards personalized data, ultimately leading to the establishment of soft tissue rupture simulation as a key tool in medical monitoring and planning of surgical intervention.

References

1. T.L. Anderson, *Fracture Mechanics: Fundamentals and Applications*, 3rd edn. (CRC Press, Taylor & Francis Group, Boca Raton, FL, 2005)
2. F. Armero, K. Garikipati, An analysis of strong discontinuities in multiplicative finite strain plasticity and their relation with the numerical simulation of strain localization in solids. *Int. J. Solids Struct.* **33**, 2863–2885 (1996)
3. G.I. Barenblatt, The formation of equilibrium cracks during brittle fracture. General ideas and hypothesis. Axially symmetric cracks. *J. Appl. Math. Mech.* **23**, 622–636 (1959)
4. G.I. Barenblatt, The mathematical theory of equilibrium cracks in brittle fracture. *Adv. Appl. Mech.* **7**, 55–129 (1962)
5. T. Belytschko, T. Black, Elastic crack growth in finite elements with minimal remeshing. *Int. J. Numer. Meth. Eng.* **45**, 601–620 (1999)
6. T. Belytschko, Y.Y. Lu, L. Gu, Element-free Galerkin methods. *Int. J. Numer. Meth. Eng.* **37**, 229–256 (1994)
7. M.A. Biot, *Mechanics of Incremental Deformations* (Wiley, New York, 1965)
8. B. Bourdin, G.A. Francfort, J.-J. Marigo, Numerical experiments in revisited brittle fracture. *J. Mech. Phys. Solids* **48**, 797–826 (2000)
9. B. Bourdin, G.A. Francfort, J.-J. Marigo, *The Variational Approach to Fracture* (Springer, Berlin, 2008)
10. A. Braides, *Gamma-Convergence for Beginners* (Oxford University Press, New York, 2002)
11. G.T. Camacho, M. Ortiz, Computational modelling of impact damage in brittle materials. *Int. J. Solids Struct.* **33**, 2899–2938 (1996)
12. F.J. Criado, Aortic dissection: a 250-year perspective. *Tex. Heart Inst. J.* **38**, 694–700 (2011)
13. H. Dal, Quasi-incompressible and quasi-inextensible element formulation for transversely anisotropic materials. *Int. J. Numer. Meth. Eng.* (2017). Submitted

14. E.A. de Souza Neto, D. Perić, D.R.J. Owen, *Computational Methods for Plasticity: Theory and Applications* (Wiley, Chichester, 2008)
15. D.S. Dugdale, Yielding of steel sheets containing slits. *J. Mech. Phys. Solids* **8**, 100–104 (1960)
16. A. Ferrara, A. Pandolfi, Numerical modeling of fracture in human arteries. *Comput. Methods Biomech. Biomed. Eng.* **11**, 553–567 (2008)
17. A. Ferrara, A. Pandolfi, A numerical study of arterial media dissection processes. *Int. J. Fract.* **166**, 21–33 (2010)
18. P.J. Flory, Thermodynamic relations for highly elastic materials. *Trans. Faraday Soc.* **57**, 829–838 (1961)
19. G.A. Francfort, J.-J. Marigo, Revisiting brittle fracture as an energy minimization problem. *J. Mech. Phys. Solids* **46**, 1319–1342 (1998)
20. T.C. Gasser, G.A. Holzapfel, Modeling 3D crack propagation in unreinforced concrete using PUFEM. *Comput. Meth. Appl. Mech. Eng.* **194**, 2859–2896 (2005)
21. T.C. Gasser, G.A. Holzapfel, Modeling the propagation of arterial dissection. *Eur. J. Mech. A/Solids* **25**, 617–633 (2006)
22. A.A. Griffith, The phenomena of rupture and flow in solids. *Phil. Trans. R. Soc. Lond. A* **221**, 163–197 (1921)
23. O. Gültekin, A Phase Field Approach to the Fracture of Anisotropic Medium. Master's thesis, University of Stuttgart, Institute of Applied Mechanics (CE), Pfaffenwaldring 7, Stuttgart, 2014
24. O. Gültekin, H. Dal, G.A. Holzapfel, A phase-field approach to model fracture of arterial walls: theory and finite element analysis. *Comput. Meth. Appl. Mech. Eng.* **312**, 542–566 (2016)
25. O. Gültekin, H. Dal, G.A. Holzapfel, Numerical aspects of anisotropic failure in soft biological tissues favor energy-based criteria: a rate-dependent anisotropic crack phase-field model. *Comput. Meth. Appl. Mech. Eng.* (2017). Submitted
26. V. Hakim, A. Karma, Laws of crack motion and phase-field models of fracture. *J. Mech. Phys. Solids* **57**, 342–368 (2009)
27. B. Halphen, Q.S. Nguyen, Sur les matériaux standard généralisés. *J. de Mécanique* **14**, 39–63 (1975)
28. R. Hill, A theory of the yielding and plastic flow of anisotropic metals. *Proc. R. Soc. Lond. A* **193**, 281–297 (1948)
29. G.A. Holzapfel, *Nonlinear Solid Mechanics A Continuum Approach for Engineering* (Wiley, Chichester, 2000)
30. G.A. Holzapfel, T.C. Gasser, R.W. Ogden, A new constitutive framework for arterial wall mechanics and a comparative study of material models. *J. Elasticity* **61**, 1–48 (2000)
31. G.A. Holzapfel, C.A.J. Schulze-Bauer, M. Stadler, Mechanics of angioplasty: wall, balloon and stent, in *Mechanics in Biology*, ed. by J. Casey, G. Bao, New York, AMD-Vol. 242/BED-Vol. 46 (The American Society of Mechanical Engineers (ASME), 2000), pp. 141–156
32. G.A. Holzapfel, G. Sommer, P. Regitnig, Anisotropic mechanical properties of tissue components in human atherosclerotic plaques. *J. Biomech. Eng.* **126**, 657–665 (2004)
33. J.D. Humphrey, G.A. Holzapfel, Mechanics, mechanobiology, and modeling of human abdominal aorta and aneurysms. *J. Biomech.* **45**, 805–814 (2012)
34. J.D. Hutcheson, C. Goettsch, S. Bertazzo, N. Maldonado, J.L. Ruiz, W. Goh, K. Yabusaki, T. Faits, C. Bouten, G. Franck, T. Quillard, P. Libby, M. Aikawa, S. Weinbaum, E. Aikawa, Genesis and growth of extracellular-vesicle-derived microcalcification in atherosclerotic plaques. *Nat. Mater.* **15**, 335–343 (2016)
35. J.W. Hutchinson, Singular behaviour at the end of a tensile crack in a hardening material. *J. Mech. Phys. Solids* **16**, 13–31 (1968)
36. G.R. Irwin, Fracture dynamics, in *Fracturing of Metals*, pp. 147–166, Cleveland, OH (American Society for Metals, 1948)
37. X. Jin, G.R. Joldes, K. Miller, K.H. Yang, A. Wittek, Meshless algorithm for soft tissue cutting in surgical simulation. *Comput. Methods Biomech. Biomed. Eng.* **17**, 800–811 (2014)
38. T. Katayama, N. Sakoda, F. Yamamoto, M. Ishizaki, Y. Iwasaki, Balloon rupture during coronary angioplasty causing dissection and intramural hematoma of the coronary artery; a case report. *J. Cardio. Cases* **1**, e17–e20 (2010)

39. J.H. Kim, S. Avril, A. Duprey, J.P. Favre, Experimental characterization of rupture in human aortic aneurysms using a full-field measurement technique. *Biomech. Model. Mechanobiol.* **11**, 841–853 (2012)
40. J.K. Lee, L. Yao, C.T. Phelps, C.R. Wirth, J. Czajka, J. Lozman, Anterior cruciate ligament tears: MR imaging compared with arthroscopy and clinical tests. *Radiology* **166**, 861–864 (1988)
41. P. Libby, P.M. Ridker, G.K. Hansson, Progress and challenges in translating the biology of atherosclerosis. *Nature* **473**, 317–325 (2011)
42. L.D. Libersky, A.G. Petschek, Smooth particle hydrodynamics with strength of materials, in *Advances in the Free-Lagrange Method Including Contributions on Adaptive Gridding and the Smooth Particle Hydrodynamics Method, Proceedings of the Next Free-Lagrange Conference*, ed. by H.E. Trease, M.F. Fritts, W.P. Crowley (Springer, 1990), pp. 248–257
43. M. Marino, G. Vairo, Influence of inter-molecular interactions on the elasto-damage mechanics of collagen fibrils: A bottom-up approach towards macroscopic tissue modeling. *J. Mech. Phys. Solids* **73**, 38–54 (2014)
44. J.E. Marsden, T.J.R. Hughes, *Mathematical Foundations of Elasticity* (Dover, New York, 1994)
45. J.M. Melenk, I. Babuška, The partition of unity finite element method: Basic theory and applications. *Comput. Meth. Appl. Mech. Eng.* **139**, 289–314 (1996)
46. C. Miehe, Aspects of the formulation and finite element implementation of large strain isotropic elasticity. *Int. J. Numer. Meth. Eng.* **37**, 1981–2004 (1994)
47. C. Miehe, H. Dal, L.-M. Schänzel, A. Raina, A phase-field model for chemo-mechanical induced fracture in lithium-ion battery electrode particles. *Int. J. Numer. Meth. Eng.* **106**, 683–711 (2016)
48. C. Miehe, M. Hofacker, L.-M. Schänzel, F. Aldakheel, Phase field modeling of fracture in multi-physics problems. Part II. Coupled brittle-to-ductile failure criteria and crack propagation in thermo-elastic-plastic solids. *Comput. Meth. Appl. Mech. Eng.* **294**, 486–522 (2015)
49. C. Miehe, M. Hofacker, F. Welschinger, A phase field model for rate-independent crack propagation: Robust algorithmic implementation based on operator splits. *Comput. Meth. Appl. Mech. Eng.* **199**, 2765–2778 (2010)
50. C. Miehe, L.-M. Schänzel, Phase field modeling of fracture in rubbery polymers. Part I. Finite elasticity coupled with brittle fracture. *J. Mech. Phys. Solids* **65**, 93–113 (2014)
51. C. Miehe, L.-M. Schänzel, H. Ulmer, Phase field modeling of fracture in multi-physics problems. Part I. Balance of crack surface and failure criteria for brittle crack propagation in thermo-elastic solids. *Comput. Meth. Appl. Mech. Eng.* **294**, 449–485 (2015)
52. C. Miehe, F. Welschinger, M. Hofacker, Thermodynamically consistent phase-field models of fracture: Variational principles and multi-field FE implementations. *Int. J. Numer. Meth. Eng.* **83**, 1273–1311 (2010)
53. N. Moës, T. Belytschko, Extended finite element method for cohesive crack growth. *Engr. Fract. Mech.* **69**, 813–833 (2002)
54. N. Moës, J. Dolbow, T. Belytschko, A finite element method for crack growth without remeshing. *Int. J. Numer. Meth. Eng.* **46**, 131–150 (1999)
55. A. Needleman, Micromechanical modeling of interfacial decohesion. *Ultramicroscopy* **40**, 203–214 (1992)
56. M. Ortiz, A. Pandolfi, Finite-deformation irreversible cohesive elements for three-dimensional crack-propagation analysis. *Int. J. Numer. Meth. Eng.* **44**, 1267–1282 (1999)
57. A. Raina, C. Miehe, A phase-field model for fracture in biological tissues. *Biomech. Model. Mechanobiol.* **15**, 479–496 (2016)
58. M.K. Rausch, G.E. Karniadakis, J.D. Humphrey, Modeling soft tissue damage and failure using a combined particle/continuum approach. *Biomech. Model. Mechanobiol.* **16**, 249–261 (2017)
59. J.R. Rice, A path independent integral and approximate analysis of strain concentration by notches and cracks. *J. Appl. Mech.* **35**, 379–386 (1968)
60. J.R. Rice, G.F. Rosengren, Plane strain deformation near a crack tip in a power-law hardening material. *J. Mech. Phys. Solids* **16**, 1–12 (1968)

61. P. Sharma, N. Maffulli, Tendon injury and tendinopathy: healing and repair. *J. Bone Joint Surg.* **87**, 187–202 (2005)
62. V.R. Sherman, W. Yang, M.A. Meyers, The material science of collagen. *J. Mech. Behav. Biomed. Mater.* **52**, 22–50 (2015)
63. S.A. Silling, Reformulation of elasticity theory for discontinuities and long-range forces. *J. Mech. Phys. Solids* **48**, 175–209 (2000)
64. S.A. Silling, E. Askarib, A meshfree method based on the peridynamic model of solid mechanics. *Comput. Struct.* **83**, 1526–1535 (2005)
65. J.C. Simo, J. Oliver, F. Amero, An analysis of strong discontinuities induced by strain softening in rate-independent inelastic solids. *Comput. Mech.* **12**, 277–296 (1993)
66. G. Sommer, T.C. Gasser, P. Regitnig, M. Auer, G.A. Holzapfel, Dissection properties of the human aortic media: an experimental study. *J. Biomech. Eng.* **130**, 021007-1–12 (2008)
67. S.W. Tsai, H.T. Hahn, *Introduction to Composite Materials* (Technomic Publishing Company, Lancaster, 1980)
68. S.W. Tsai, E.M. Wu, A general theory of strength of anisotropic materials. *J. Compos. Mater.* **5**, 58–80 (1971)
69. G.N. Wells, Discontinuous Modelling of Strain Localization and Failure. PhD thesis, Delft University of Technology, Netherlands, 2001
70. H.M. Westergaard, Bearing pressures and cracks. *J. Appl. Mech.* **6**, 49–53 (1939)
71. P. Wriggers, *Nonlinear Finite Element Methods* (Springer-Verlag, Berlin Heidelberg, 2008)
72. X.-P. Xu, A. Needleman, Numerical simulations of fast crack growth in brittle solids. *J. Mech. Phys. Solids* **42**, 1397–1434 (1994)